



Transition metal embedded two-dimensional C₃N as highly active electrocatalysts for oxygen evolution and reduction reactions

Journal:	<i>Journal of Materials Chemistry A</i>
Manuscript ID	TA-ART-02-2019-001389.R1
Article Type:	Paper
Date Submitted by the Author:	02-Apr-2019
Complete List of Authors:	Zhou, Yanan; Sichuan University, ; E O Lawrence Berkeley National Laboratory, Gao, Guoping; Lawrence Berkeley National Laboratory, Berkeley, Kang, Jun; E O Lawrence Berkeley National Laboratory, Materials Sciences Division Chu, Wei; Sichuan University, Chemical Engineering Department Wang, Lin-Wang; Lawrence Berkeley National Laboratory,



Transition metal embedded two-dimensional C₃N as highly active electrocatalysts for oxygen evolution and reduction reactions

Yanan Zhou,^{ab} Guoping Gao,^b Jun Kang,^b Wei Chu,^{*a} and Lin-Wang Wang^{*b}

Received 00th January 20xx,
Accepted 00th January 20xx

DOI: 10.1039/x0xx00000x

www.rsc.org/

Searching for the highly efficient, stable and cost-effective catalysts for oxygen evolution reaction (OER) and oxygen reduction reaction (ORR) are vital to resolve energy security and environmental problems. Herein, by means of the computational screening based on density functional theory (DFT), we studied a wide range of transition metal (TM) atom embedded into double carbon vacancy of C₃N monolayer (V_{CC}), denoted as TM-V_{CC} (TM= Mn, Fe, Co, Ni, Cu, Ru, Rh, Pd, Ir and Pt), as efficient single-atom catalysts (SACs) for OER and ORR. The calculated results show that all the considered TM-V_{CC} composites exhibit metallic feature that ensures the efficient charge transfer during reactions. The interaction strength between intermediates and TM-V_{CC} has a direct correlation with the d-band center of TM, which can be tuned by changing the TM atoms with the different number of d-electron. The best catalyst for OER is Rh-V_{CC} with an overpotential (η^{OER}) of 0.35 V, followed by Co-V_{CC} (0.43 V). For ORR process, Rh-V_{CC} exhibits the lowest ORR overpotential (η^{ORR}) of 0.27 V, followed by Co-V_{CC} (0.42 V). The results suggest that the performance of the newly predicted Rh-V_{CC} and Co-V_{CC} SACs is comparable to those of the noble-metal benchmark catalysts for OER and ORR. Ab initio molecular dynamics simulation exhibits that the Rh-V_{CC} and Co-V_{CC} SACs can remain stable under 300K, and possess high energy barriers to prevent the isolated Rh and Co atoms from clustering. Our results highlight a new family of efficient and stable catalysts with single-atom anchored on carbon nitride-based materials, which provides a useful guideline for catalyst design and practical application.

1. Introduction

The growing global energy crisis and environmental pollution problem have stimulated tremendous interest in researches on sustainable energy storage and conversion systems.¹⁻³ Promising technologies include fuel cells,⁴ water splitting⁵ and metal-air batteries⁶ owing to their high energy density and environmental benign. The electrocatalytic oxygen evolution reaction (OER) and oxygen reduction reaction (ORR) play important roles in the electrochemical energy

conversion processes. As we known, the OER occurs on the anode side of electrochemical water splitting cell with ruthenium (Ru) and iridium (Ir) oxides as the state-of-the-art electrocatalysts,^{7, 8} while the ORR, a reverse reaction of the OER, happens on the cathode side of the fuel cell and the air battery with the platinum (Pt) and its alloys as the most active catalysts.⁹⁻¹¹ However, due to the multistep holes transport requirement, and the insulating nature for some of these oxide catalysis, the reaction can be sluggish even for some of these noble metal catalysts. Furthermore, the high cost and limited availability of these noble metals make it highly desirable to use common metal replacement. The recent research of using common transition metal embedded in two-dimensional materials open new revenue for searching such alternative catalysts.

Since the discovery of graphene,¹² two-dimensional (2D) materials such as hexagonal boron nitride (*h*-BN),^{13, 14} MXenes¹⁵⁻¹⁷ and phosphorene^{18, 19} have attracted intense attention in both experiment and

^a School of Chemical Engineering, Sichuan University, Chengdu, 610065, Sichuan, China

^b Materials Science Division, Lawrence Berkeley National Laboratory, Berkeley, 94720, California, United States

*E-mail address: chuwei1965@scu.edu.cn (Wei Chu); lwwang@lbl.gov (Lin-Wang Wang)

†Electronic Supplementary Information (ESI) available: [details of any supplementary information available should be included here]. See DOI: 10.1039/x0xx00000x

theory as promising catalysts for energy conversion and storage applications. Notably, carbon-based materials were widely investigated as active OER and ORR catalysts due to their conductivity, low cost and wide use in electrochemistry.²⁰⁻²² It is known that introducing heteroatoms in graphene can significantly enhance its OER and ORR activity.²³⁻²⁶ Examples include metal-nitrogen carbon (M-N-C) materials, like Co-N-C and Fe-N-C complexes.²⁷⁻²⁹ However, they generally need advanced synthetic approaches techniques, and might be limited to a few transition metal elements. Another approach is to doping the 2D material with transition metals. Such single embedded atom can be behaved as catalytic center, and it provides another possible approach to search for new catalysts for OER and ORR reactions. The single-atom catalysts (SACs) can provide the tunable number of active sites and promise the use of minimum amount of transition metals. This approach also provides a large designing space in terms of the type of transition metal and their concentrations. It has been recently become a very active area of research.^{30, 31}

Some of the early works were focused on doping pure graphene. However, it is found that pure graphene cannot bind with transition metal strong enough. Thus, some nitrogen is always introduced around the vacancy. However, recently, a new graphene-like 2D polyaniline (C_3N) material was successfully synthesized in experiment using a bottom-up wet-chemical reaction, which contains uniformly distributed C and N atoms within a unit cell of the 2D crystal.³² Compared to other 2D carbonitrides, e.g., C_3N_4 and C_2N , the C_3N has the original structure of graphene, thus could be mechanically more robust. This is indeed confirmed by theoretically calculation.^{33, 34} In addition, it also has suitable bandgap and superior thermal conductivity. The monolayer C_3N and its derivatives have also been predicted to be suitable for gas sensor and capture,^{35, 36} and Na- and K-ion batteries.³⁷ Baek et al. synthesized C_3N as anode material for Li-ion batteries,³⁸ and observed excellent electrochemical performance. Most recently, using first-principle calculations, Yang et al. found that doped C_3N monolayer with B replacing C is more active toward ORR than B replacing N in the acid environment.³⁹ All these previous works indicate that C_3N could be an excellent candidate as a substrate for SACs. The pre-existence of N in the system makes it unnecessary to introduce additional N when dope the system with TM. Nevertheless, so far, there is a lack of systematic theoretical investigation on the using of C_3N as the substrate for SACs. Such theoretical investigation is necessary given the tremendous speed of progress in the experimental work in this field. The binding strength between perfect C_3N -monolayer and TM atoms is weak.⁴⁰ It thus necessary to introduce defects

in C_3N monolayer, which allows the formation of dispersed single-metal electrocatalyst for OER/ORR. As well known, defect is extremely important, and very often it is what makes a semiconductor material works in terms of controlling the property of the material.⁴¹ Experimental studies have shown that using electron or ion irradiation technology, one could create vacancies on carbon-based materials.⁴² Such vacancies can act as binding sites for TM atoms.^{43, 44} Thus, in this work, we will study defect site binding with TM atoms to be used as SACs in C_3N monolayer for OER and ORR. We will focus on late transition metals starting from Mn, including Fe, Co, Ni, Cu, Ru, Rh, Pd, Ir and Pt, as these elements have shown OER and ORR activities in various materials.⁴⁵⁻⁴⁷

More specifically, we will design a series of atomically dispersed TM atoms adsorbed on the double-carbon vacancy site of the C_3N monolayer and systematically investigated their catalytic activities toward OER and ORR. The double-carbon vacancy is necessarily since a single atom vacancy will not be large enough to accommodate a TM. On the other hand, losing one N atom at the defect site will not be ideal since it will reduce the binding energy of the TM at the defect site. Thus, as we will show, the formation energy of double-carbon vacancy is smaller than the C-N vacancy, which makes the double-carbon vacancy more likely to be formed. The metallic properties of all considered TM- V_{CC} composites indicate that the charge transfer during the reactions should be efficient. We found strong correlation between the catalytic activities for OER, and ORR and the d-electron numbers of the doped TM atoms. Notably, our results show that Rh- V_{CC} would be the best catalyst for OER with overpotential (η^{OER}) of 0.35 V, followed by Co- V_{CC} (0.43 V). Moreover, Rh- V_{CC} is the best catalyst for ORR with the lowest ORR overpotential (η^{ORR}) of 0.27 V, followed by Co- V_{CC} (0.42 V).

2. Computational methodology

All the calculations were carried out by the Vienna ab initio Simulation Package (VASP)^{48, 49} using density functional theory (DFT) method. The projector augmented wave (PAW) potentials were employed to describe the nuclei–electron interactions.⁵⁰ The generalized gradient approximation (GGA)⁵¹ with the PerdewBurke-Ernzerhof (PBE)⁵² functional was used to describe the electron exchange-correlation interactions. Grimme's DFT-D3 correction method was used to account for the van der Waals (vdW) effects.⁵³ Spin polarization was considered throughout all the calculations. The wavefunctions of valence electrons were expanded by plane wave basis set with a cutoff energy of 500 eV. The convergence criterion for energy and force during geometrical optimization

was set to 10^{-5} eV and 10^{-2} eV/Å, respectively. The vacuum space of 20 Å was applied to avoid the interactions along the z-direction. The Brillouin zone was sampled by a 3x3x1 Monkhorst-Pack mesh grid for the structural optimization.⁵⁴ The climbing image nudged elastic band (CINEB) method^{55, 56} was used to explore the TM diffusion barrier. Ab initio molecular dynamics (AIMD) simulations were also performed to examine their dynamical stability, and the algorithm of the Nose thermostat was carried out to simulate a canonical ensemble,⁵⁷ under 300K for 10ps with a time step of 2fs. Throughout the calculation, for aqueous based materials, we have also used implicit solvent model to account for the effects of polarization due to the water condition that calculated with VASPsol with the dielectric constant set to 78.4.⁵⁸

In the acidic environment, the OER proceeds have been proposed via a four-stage pathway.^{45, 59, 60} In this pathway, there are four intermediate states. They are: initiate state with the bare surface (denoted as *); the state with one HO binding to the surface (denoted as HO*); the state with one O binding on the surface (denoted as O*); the state with HOO binding to the surface (denoted as HOO*). From one intermediate state to the next intermediate state, the system either takes one H₂O molecule and releases one H⁺ (in the acid case), or take one OH⁻ (in the alkali case), or simply release one H⁺. In all these cases, each step will release one hole charge from the electrode Fermi energy to the solvent. The fourth intermediate state can go back to the first intermediate state by releasing one O₂ molecule, one H⁺ and one electron. These four steps can be written as:



where * stands for catalyst and adsorption site on the catalyst, (l) and (g) refer to the liquid and gas phase, respectively. On the other hand, the Gibbs free energies corresponding to the four intermediate states (using the first state as the reference energy) will be:

$$\Delta G_* = 0 \quad (2\text{a})$$

$$\Delta G_{\text{HO}^*} = G_{\text{HO}^*} + G_{\text{H}^+} + \mu_{\text{e}^-} - G_* - G_{\text{H}_2\text{O},\text{l}} \quad (2\text{b})$$

$$\Delta G_{\text{O}^*} = G_{\text{O}^*} + 2G_{\text{H}^+} + 2\mu_{\text{e}^-} - G_* - G_{\text{H}_2\text{O},\text{l}} \quad (2\text{c})$$

$$\Delta G_{\text{HOO}^*} = G_{\text{HOO}^*} + 3G_{\text{H}^+} + 3\mu_{\text{e}^-} - G_* - 2G_{\text{H}_2\text{O},\text{l}} \quad (2\text{d})$$

$$\Delta G_{*+\text{O}_2} = G_{\text{O}_2} + 4G_{\text{H}^+} + 4\mu_{\text{e}^-} - 2G_{\text{H}_2\text{O},\text{l}} \quad (2\text{e})$$

The last equation Eq.(2e) represents the situation when one oxygen molecule is generated, and the system goes back to its initial state (*). Note these intermediate states Gibbs free energies depend on the chemical potential of H⁺ in the water: G_{H^+} (hence, the pH values), as well as the electrode Fermi energy μ_{e^-} . We will study the pH=0 case, and use the standard Hydrogen generation electrode (SHE) as the reference for electrode Fermi energy. Hence, $\mu_{\text{e}^-} = \mu_{\text{SHE}} - U$ (we have used a negative sign here to be consistent with the convention, and make U positive). Since at pH=0, we have: $G_{\text{H}^+} + \mu_{\text{SHE}} = 1/2G_{\text{H}_2}$, the above equations can be converted into:

$$\Delta G_* = 0 \quad (3\text{a})$$

$$\Delta G_{\text{HO}^*} = G_{\text{HO}^*} + 0.5G_{\text{H}_2,\text{g}} - U - G_* - G_{\text{H}_2\text{O},\text{l}} \quad (3\text{b})$$

$$\Delta G_{\text{O}^*} = G_{\text{O}^*} + G_{\text{H}_2,\text{g}} - 2U - G_* - G_{\text{H}_2\text{O},\text{l}} \quad (3\text{c})$$

$$\Delta G_{\text{HOO}^*} = G_{\text{HOO}^*} + 1.5G_{\text{H}_2,\text{g}} - 3U - G_* - 2G_{\text{H}_2\text{O},\text{l}} \quad (3\text{d})$$

$$\Delta G_{*+\text{O}_2} = 4 * 1.23 \text{ eV} - 4U \quad (3\text{e})$$

In writing down the Eq.(3e), we have used the experimental fact: $G_{\text{O}_2} + 4G_{\text{H}_2} - 2G_{\text{H}_2\text{O},\text{l}} = 4 * 1.23 \text{ eV}$, so we don't need to calculate the free energy of O₂ in the gas phase due to the poorly description of this DFT calculation. It is difficult to calculate directly the Gibbs free energy of the liquid phase $G_{\text{H}_2\text{O},\text{l}}$. It is customary to calculate the Gibbs free energy of liquid phase from its vapor phase counterpart at their equilibrium pressure when they have the same Gibbs free energies. Thus, $G_{\text{H}_2\text{O},\text{l}} = E_{\text{H}_2\text{O}} + \text{ZPE}_{\text{H}_2\text{O}} - \text{TS}_{\text{H}_2\text{O}}$. Here, $E_{\text{H}_2\text{O}}$ is the total energy of single water molecule in gas phase obtained directly from DFT calculation; $\text{ZPE}_{\text{H}_2\text{O}}$ is the zero point free energy; T is the temperature of 298.15 K, $\text{TS}_{\text{H}_2\text{O}}$ is the entropy term of the gas phase, it is 0.67 eV.⁶¹ Similarly for $G_{\text{H}_2,\text{g}} = E_{\text{H}_2} + \text{ZPE}_{\text{H}_2} - \text{TS}_{\text{H}_2}$, E_{H_2} is the DFT energy of H₂ molecule in vacuum, and the ZPE_{H_2} is the zero energy of the frequency vibration. The TS_{H_2} are calculated with the value of 0.41 eV in Ref.⁶¹ The same is true to the other few adsorbed adsorbates X (X=HO*, O* and HOO*), where $G_{\text{X}^*} = E_{\text{X}^*} + \text{ZPE}_{\text{X}^*} - \text{TS}_{\text{X}^*}$. Here E_{X^*} is the DFT total energy of the X* system after taking into account the solvent polarization effect using the implicit solvent model. ZPE_{X^*} is the ZPE of X* calculated from its phonon modes. Here we only include the phonon degree of freedom in X*, while keeping the catalyst * fixed during frequency calculation. TS_{X^*} is the entropy energy of the adsorbed adsorbates obtained from the frequency vibration calculation. The zero-point energies corrections and the entropies contributions of the adsorbates (HO*, O* and HOO*) on the Co-V_{CC} and Rh-V_{CC} are listed in **Table S1 and S2**. Finally, $G_* = E_*$ refers to the DFT

ARTICLE

calculated total energy of catalyst substrate using the implicit solvent model. Note that for all the above calculations, we have ignored the thermal energy term in the evaluation of G due to the phonon degree of freedom. That energy can be calculated from the phonon model, just like the TS term, but it is rather small, thus has been ignored.

After having a way to calculate the intermediate state Gibbs free energies, the reaction criterion from one state to a subsequent state in the OER reaction is to increase the voltage U , so the Gibbs free energy of the subsequent step becomes lower than the previous step. This also implies that ΔG_{*+O_2} must be smaller than ΔG^* . Thus, the minimum possible U is 1.23 V. Besides, this can only happen when the Gibbs free energies of the four intermediate states are equal distance spaced between 0 and 4×1.23 when $U=0$. If this is not true, then the maximum (U_{\max}) value of all the four steps for their reactions to happen is the bottleneck of the whole OER. The $\eta^{\text{OER}}=U_{\max}-1.23$ is called the overpotential of OER. The goal of OER optimization is to reduce this over potential as much as possible.

The ORR is just the inverse reaction of OER. Here the U which makes the Gibbs free energies equal to each other between two subsequent intermediate states is the voltage it generated in this chemical reaction. The minimum U_{\min} among all the four steps defined the voltage of the fuel-cell. Thus, instead of looking for U_{\max} , here we are interested in U_{\min} of the four reactions. Obviously, the maximum possible U_{\min} is also 1.23 V when all the four Gibbs free energies of Eq.(3) are equally spaced when $U=0$. $\eta^{\text{ORR}}=1.23-U_{\min}$ is call the overpotential of ORR. The goal of ORR research is also looking for the minimum ORR overpotential.

Finally, it is worth to note that, although we have tested different atomic configurations of the HO^* , O^* , HOO^* absorption on the TM-V_{CC} site, the most stable configuration always correspond to one O binding directly to the TM.

3. Results and discussion

As shown in **Fig. S1a** in the Supporting Information, there are six C and two N atoms in the primitive unit cell of $\text{p-C}_3\text{N}$. The optimized crystal lattice parameter of $\text{p-C}_3\text{N}$ is 4.86 Å, and the bond length of C-C and C-N are both about 1.41 Å, in agreement with the previous results.^{33, 40, 62} There are two kinds of double vacancies in the (3×3) supercell of the C_3N monolayer, one is double carbon vacancy (V_{CC}) by removing two neighboring C atoms, the other one is vacancy CN (V_{CN}) created by removing one C atom and its neighboring N atom. The optimized stable atomic configuration for the (3×3) $\text{p-C}_3\text{N}$, V_{CC} and V_{CN}

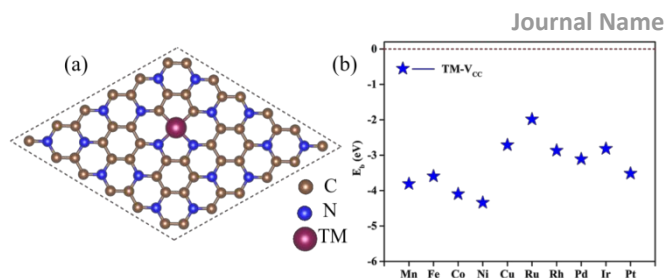


Fig. 1 (a) Top view of TM-V_{CC} monolayer, (b) Binding energies of various transition metals anchored on the V_{CC} systems.

nanosheets are exhibited in **Fig. S1b-d**, respectively. It can be seen that there is no significant structural reconstruction around the vacancy of V_{CC} , the bond lengths of C-C and C-N around the vacancy stretch to 2.75 and 2.47 Å, respectively. While, for V_{CN} , one pentagon and one hendecagon rings are formed around the vacancy. The vacancy formation energy (E_f) is a key physical parameter to describe the stability of point defects in C_3N monolayer, and defined as $E_f = E_V - E_P + \mu_{\text{host}}$.^{63, 64} In this equation, E_V and E_P are the total energies of the defective and perfect (3×3) C_3N sheets, respectively. μ_{host} is the chemical potential of the removed C or N atom, determined by the total energy per atom in perfect graphene or in a N_2 molecule, respectively. The calculated formation energies for V_{CC} and V_{CN} are 4.88 and 6.27 eV, respectively, which agrees well with the reported result,⁶⁵ suggesting that the V_{CC} vacancy is thermodynamically favored over V_{CN} . Compared to the formation energy of the double vacancy in graphene (7.26 eV),⁶⁶ the much smaller formation energy of the V_{CC} indicates that the formation of V_{CC} in the C_3N monolayer is thermodynamically more favorable.⁶⁷ Therefore, we did the following works based on the V_{CC} defect. Electronic conductivity is one of the key factors in determining the efficiency of electrode materials. Therefore the electronic structures of V_{CC} will be studied. For comparison, the density of states (DOS) of $\text{p-C}_3\text{N}$ and V_{CC} monolayers are exhibited in **Fig. S2a**, The DOS shows that $\text{p-C}_3\text{N}$ is a nonmagnetic indirect semiconductor with a band gap about 0.37 eV at the PBE level calculation in line with previous results.^{39, 65} Seen from **Fig. S2b**, in contrast to $\text{p-C}_3\text{N}$, the V_{CC} is magnetic and the calculated total spin magnetic moment is 1.33 μ_B . Additionally, the electron states crossing the Fermi levels suggests a good electric conductivity of V_{CC} if there are sufficient concentration of it, which makes it suitable for electrode.

The vacancy region of V_{CC} is expected to bind metal atoms tightly as the substrate for SACs (**Fig. 1a**). First, we calculated the binding energies for vary TM atoms on the V_{CC} from Mn to Cu, and some noble metal atoms such as Ru, Rh, Pd, Ir and Pt are also taken into consideration in our investigation. The binding energy is defined as $E_b = E_{\text{TM-V}_{\text{CC}}} - \mu_{\text{TM}} - E_{\text{V}_{\text{CC}}}$,

where $E_{\text{TM-V}_{\text{CC}}}$ and $E_{\text{V}_{\text{CC}}}$ are the total energies of the TM-V_{CC} system, and V_{CC} substrate, respectively. μ_{TM} is the chemical potential of the TM atom computed from the elemental bulk crystal. Since the μ_{TM} is referenced with respect to its bulk metal, negative values of E_{b} (Fig. 1b) indicates that the TM atoms in V_{CC} are stable against clustering.⁶⁸ The optimized configurations of TM-V_{CC} are exhibited in Fig. S3, we can see that all the TM atoms prefer to be adsorbed on the vacancy area.

The distinct electronic structures for different TM atoms anchored on the V_{CC} can provide us with insights to understand their catalytic properties. The PDOS of the d orbitals of the different TM atoms anchored on V_{CC} were calculated as shown in Fig. 2. As shown in Fig. S4, all the considered TM-V_{CC} catalysts in our work show metallic properties, suggesting good electric conductivity for all the TM-V_{CC} catalysts as discussed above. The d band center position (ϵ_{d}) has been used to analyze the interaction strength between adsorbate and substrate.⁶⁹⁻⁷³ In Fig. 2, we also plotted ϵ_{d} calculated as the center of mass position of the d-band PDOS. A clear shift of ϵ_{d} to lower energy position with respect to the Fermi level is seen with the increase of the d-electron number of the TM atom. It is well known that the large number

transfer from the TM to the adsorbates. As a result, the interaction strength of adsorbates on TM-V_{CC} is expected to exhibit the following trends: Mn>Fe>Co>Ni>Cu, Ru>Rh>Pd and Ir>Pt. To verify the above prediction, we plot the Gibbs free energy of adsorbates (i.e., the intermediate state energies as calculated in Eq.(3) with U=0) with various number of d-electrons of the TM-V_{CC} systems in Fig. 3a. We can conclude that, for the TM's in the same row of the periodic table, the increase of their d-electron numbers tend to weaken the adsorption free energies of adsorbates. This is also true with the position of ϵ_{d} as shown in Fig. 3b. There is a negative correlation between ϵ_{d} and ΔG of adsorbates, as least when the TM's of the same row are used. This phenomenon was also observed experimentally⁷⁵ and in other theoretically studies.^{45, 76} Therefore, we can modulate the interaction strength to the optimal value for both OER and ORR performance by tuning the TM atom embedded into V_{CC}.

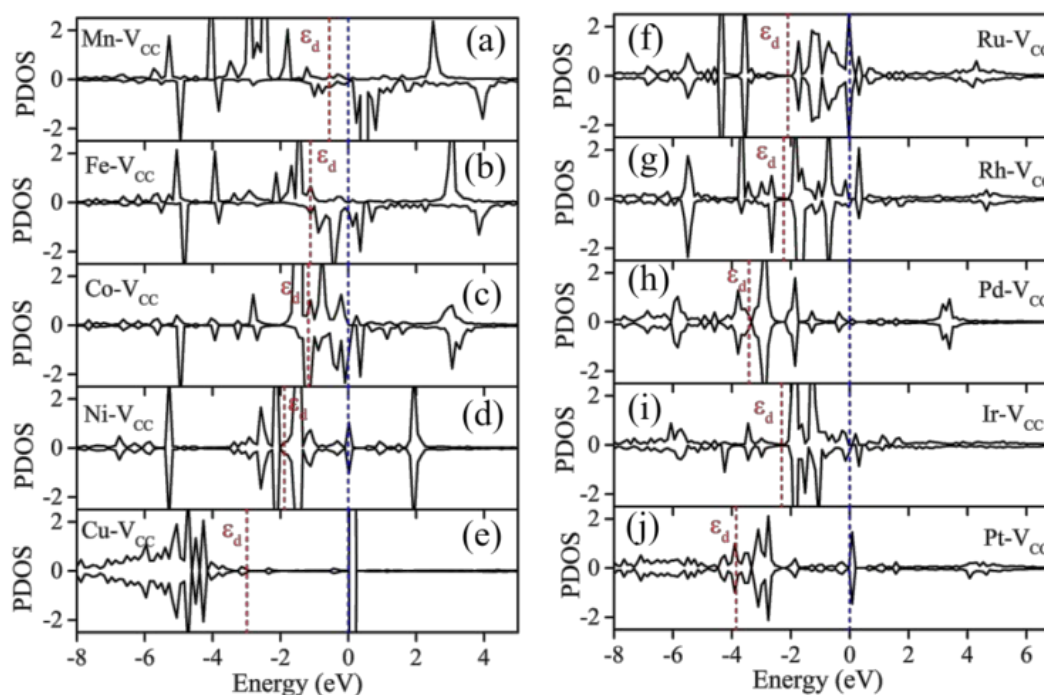


Fig. 2 Calculated PDOS of the d band in the TM-V_{CC} systems. The Fermi level is set at the zero of energy (blue dash line) and the d band center (ϵ_{d}) is marked by the red dash line.

of d-electron in the TM and lower energy level of ϵ_{d} generally result in a weaker interaction strength with HO*, O* and HOO* adsorbates.⁷⁴ This is because the interaction between the TM and the adsorbates happen by hybridization of their electronic level, and charge

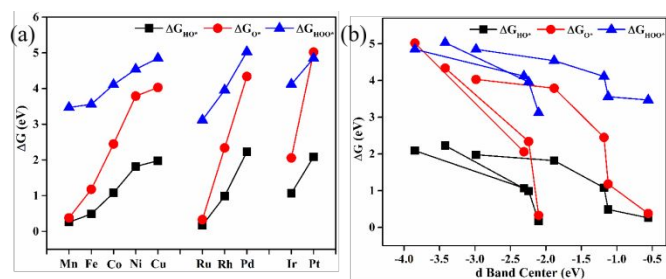


Fig. 3 (a) Gibbs free energy of adsorbates as defined in Eq.(3) (with $U=0$) with various numbers of d-electron doped TM- V_{CC} systems, and (b) Gibbs free energy of adsorbates correspond to the d band center ϵ_d

As presented above, the intermediate state Gibbs free energies of adsorbates (HO^* , O^* and HOO^*) on different TM- V_{CC} catalysts determines the distinct rate-determining step of OER and ORR. According to the Sabatier's principle,⁷⁷ too strong or too weak interaction strength between the adsorbates and catalyst both leads to the adversarial effects on OER and ORR. For an ideal catalyst, the energy distances for all the steps (between two adjacent intermediate states) are all 1.23 eV (when $U=0$). Therefore, the OER and ORR can occur at their thermodynamic limit and the overpotential η is zero. However, in reality, the energy steps are not equally distanced, which limits the reactions. While, the OER overpotential is determined by the maximum energy distance, the ORR overpotential is determined by the minimum

energy distance as discussed above. The calculated free energy diagrams for all the intermediate states of OER and ORR for each TM- V_{CC} catalyst are shown in **Fig. 4**, and the rate-determining step of each catalyst colored in red (for OER) and green (for ORR) respectively. With the increase of the d-electron number of anchored TM atoms, the Gibbs free energy of HO^* , O^* and HOO^* on TM- V_{CC} decreases accordingly (**Fig. 3a**). From the Mn- V_{CC} to Co- V_{CC} in the period four, the third step ($O^* \rightarrow HOO^*$) exhibits as the rate-determining step, and the corresponding overpotential η^{OER} decreases from 1.86 V (Mn- V_{CC}) to 0.43 V (Co- V_{CC}). However, for the Ni- V_{CC} and Cu- V_{CC} , with the further increase of the d-electron number, the second step from HO^* to O^* becomes the potential-determining step (**Fig. 4d and e**). This trend is also true for the noble metals (Ru- V_{CC} , Rh- V_{CC} , Pd- V_{CC} , Ir- V_{CC} and Pt- V_{CC} , **Fig. 4f to 4j**). Remarkably, the Rh- V_{CC} among the considered systems is predicted to possess the best OER performance with an overpotential η^{OER} of 0.35 V, this is followed by Co- V_{CC} of 0.43 V. Both of them are comparable to the calculated RuO_2 catalyst (0.42 V).⁷⁸

As we known, the ORR is the reverse reaction of the OER. With the increase number of d-electron from Mn to Co, the corresponding η^{ORR} value decreases from 1.11 eV (Mn- V_{CC}) to 0.42 eV (Co- V_{CC}). The third step ($O^* \rightarrow HO^*$), fourth step ($HO^* \rightarrow H_2O$) and the second step ($HOO^* \rightarrow O^*$) is the potential-determining step for Mn- V_{CC} , Fe- V_{CC} and Co- V_{CC} ,

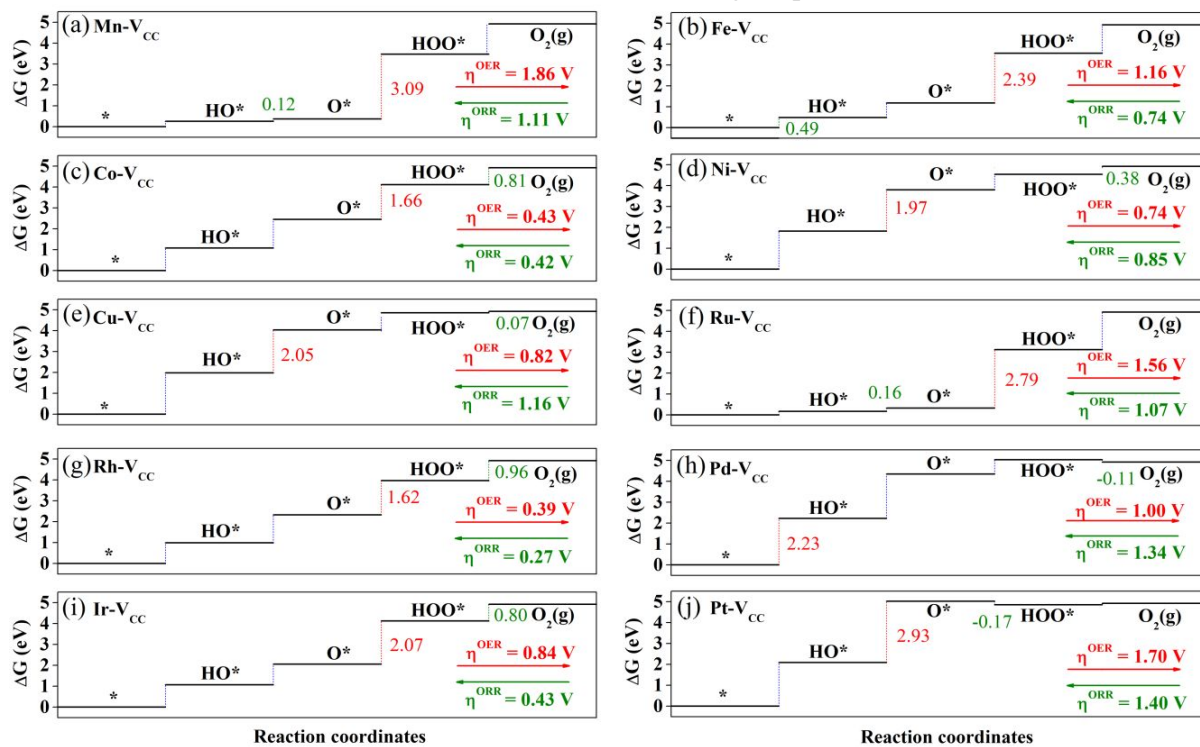


Fig. 4 The free energy diagrams of OER and ORR on TM- V_{CC} . The red and the blue dash lines are the rate-limiting step for OER and ORR, respectively.

respectively. Similar to the above OER performance, with the further increase of the d-electron number for Ni-V_{CC} and Cu-V_{CC}, the value of η^{ORR} increases

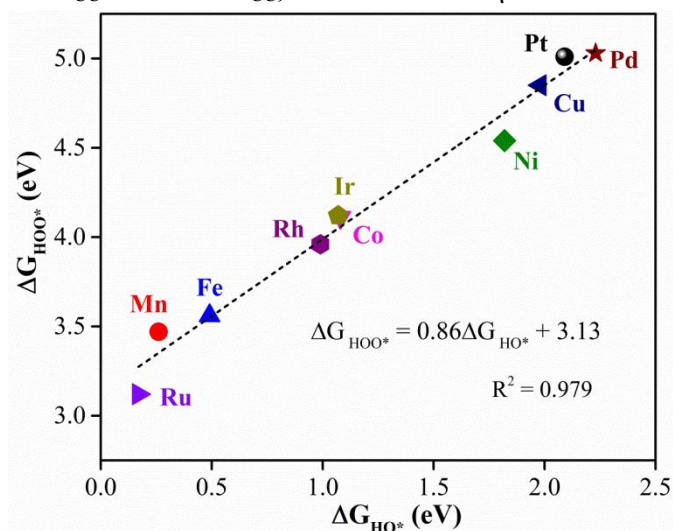


Fig. 5 The scaling relationship between ΔG_{HO^*} and ΔG_{HOO^*} on various TM-V_{CC} systems.

accordingly against the ORR performance. Among all the explored TM-V_{CC}, the best catalyst for the ORR is Rh-V_{CC} with the lowest η^{ORR} of 0.27 V, followed by Co-V_{CC} (0.42 V). Notably, both of their ORR overpotentials are lower than the reported best catalyst Pt for ORR (0.45 V)⁵⁹ based on DFT calculation. For comparison, previous findings on OER/ORR catalytic performance for the metal doped carbon materials are listed in Table S4, especially the Co- and Rh- based SACs.^{26, 45, 79}

The relationship between the Gibbs free energy of the intermediates (ΔG_{HO^*} , ΔG_{O^*} and ΔG_{HOO^*} of Eq.3 when $U=0$) can be explored to analyze the OER and ORR trends for different catalysts. By comparing the ΔG_{HO^*} and ΔG_{HOO^*} for all the calculated cases in our study, we found that ΔG_{HOO^*} can be expressed as a function of ΔG_{HO^*} via equation $\Delta G_{\text{HOO}^*}=0.86\Delta G_{\text{HO}^*}+3.13$ eV as shown in **Fig. 5**. Apparently, the free energies of adsorbed HO* and HOO* species are linearly correlated as the coefficient of determination (R^2) is 0.979. The slope close to the unity in the relationship between HO* and HOO* reflects the fact that both intermediates have a single bond between on O atom

and TM. The constant intercept implies that HO* and HOO* normally prefer the same type of adsorption site,⁷⁸ as shown in **Fig. S5 and S6**. Notably, similar relationships were also observed in carbon materials and metal surfaces.⁸⁰ Note, that, if we assume the above slope is 1, then that means the $\Delta G_{\text{HOO}^*}-\Delta G_{\text{HO}^*}$ is a constant. Given the fact, all the OER determining steps happen either at the step of HO* to O*, or O* to HOO* (with the exception of Pd, where its * to HO* step distance is almost the same as the HO* to O* distance), then the overpotential will be determined purely by the $\Delta G_{\text{O}^*}-\Delta G_{\text{HO}^*}$ distance. This is indeed true as the volcano plot shown in Figure 6a, where the overpotential falls into a line as a function of $\Delta G_{\text{O}^*}-\Delta G_{\text{HO}^*}$. The theoretical line is the dashed line in **Fig. 6a** under the assumption $\Delta G_{\text{HOO}^*}-\Delta G_{\text{HO}^*}$ is a constant. The smallest overpotential happens around Rh and Co when their $\Delta G_{\text{O}^*}-\Delta G_{\text{HO}^*}$ is close to a half of $\Delta G_{\text{HOO}^*}-\Delta G_{\text{HO}^*}$.

As mentioned above, the overpotential of ORR is determined by the minimum step distance in **Fig. 4**. We notice that, this ORR step can be approximated as either happening at the first step: * to HO* (step1), or at the last step, from HOO* to *+O₂ (step4). Note, for Mn, Ru, the determining step happen at HO* to O* step, but the * to HO* step is similarly small, thus can be approximated as the determining step. For Pt, the determining step happens at O* to HOO*, but once again the HOO* to *+O₂ step is similarly small, so can be approximated as the rate determining step. Now, if we assume $\Delta G_{\text{HOO}^*}-\Delta G_{\text{HO}^*}$ is fixed, then the step1+step4 distance is also fixed. If the ORR determining steps happens either in step1 or step4 (the minimum of them), then the ORR overpotential can be determined by the amplitude of step1 (e.g., the ΔG_{HO^*} value). Indeed, **Fig. 6b** shows the volcano plot of the ORR overpotential as a function of ΔG_{HO^*} . Theoretically, the minimum overpotential happens when ΔG_{HO^*} equals half of the step1+step4 value, as indicated by the dashed line. In reality, Rh, Co and Ir have the minimum overpotentials. The results do fall into the single line volcano curve.

Finally, to evaluate the dynamic stabilities of the efficient Co-V_{CC} and Rh-V_{CC} catalysts for both OER and ORR, the diffusion barriers of Co and Rh atoms were calculated. As shown in **Fig. S7 and S8**, to

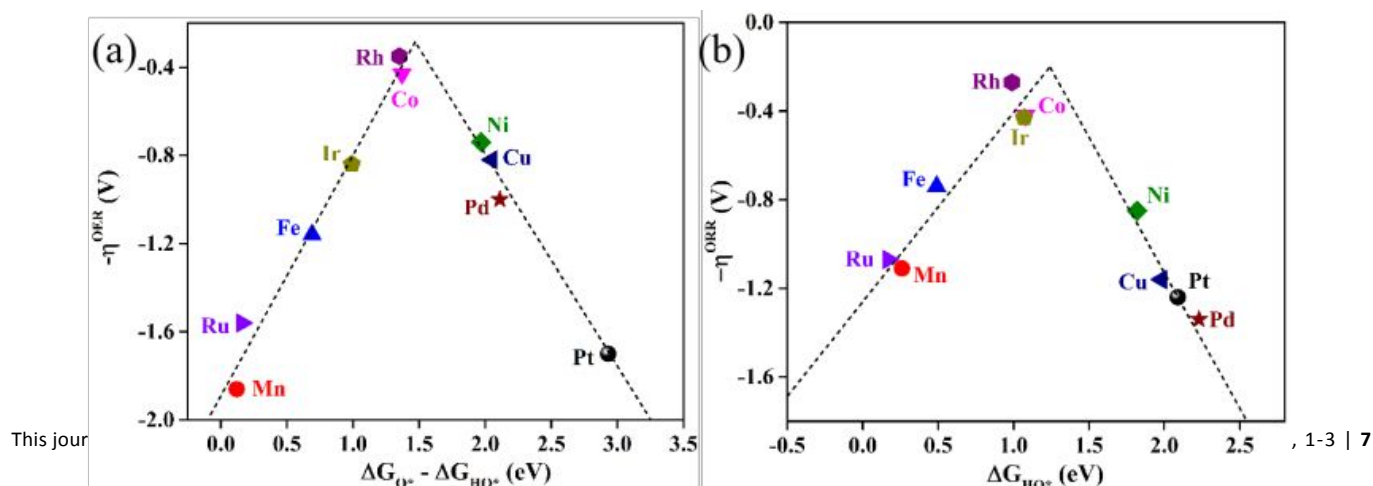


Fig. 6 (a) The calculated negative overpotential ($-\eta^{\text{ORR}}$) against $\Delta G_{\text{O}^*}-\Delta G_{\text{HOO}^*}$ on TM-V_{CC}, (b) The calculated ORR volcano curve of the $-\eta^{\text{ORR}}$ as the function of ΔG_{HO^*} on TM-V_{CC}.

diffuse from the defect adsorption site to the neighboring hollow site, Co and Rh atoms need to overcome the energy barriers of 2.47 eV and 1.96 eV, respectively, suggesting that the adsorbed Co and Rh atoms can hardly diffuse to form clusters. Moreover, the AIMD simulations results (Fig. S9) show that the energies are oscillating near the equilibrium state, indicating the kinetic stability of Co-V_{CC} and Rh-V_{CC}. Thus, Co-V_{CC} and Rh-V_{CC} are indeed highly efficient and stable single-atom catalysts for both OER and ORR.

4. Conclusions

In summary, by using computational screening method, we systematically studied a series of single transition metal atoms anchored on double carbon vacancy of C₃N monolayer as the active sites for both OER and ORR catalytic processes. It was found that increasing d-electron number can lead to the lower d-band center that weakens the interaction strength between intermediates species and the TM atoms. Thus, the ideal TM-V_{CC} catalyst for OER and ORR can be screened by adjusting the TM element. The OER overpotential η^{OER} follow a volcano plot of $\Delta G_{\text{O}^*} - \Delta G_{\text{HOO}^*}$, while the ORR overpotential η^{ORR} follow a volcano plot of ΔG_{HO^*} . Among all the studied TM-V_{CC} catalysts, the best TM atom for OER is Rh-V_{CC} with η^{OER} of 0.35 V, followed by Co-V_{CC} (0.43 V), and for ORR, Rh-V_{CC} exhibits the lowest η^{ORR} of 0.27 V, followed by Co-V_{CC} (0.42 V). It is also found that Co-V_{CC} and Rh-V_{CC} are stable against clustering and diffusion. These calculations suggest that Rh-V_{CC} and Co-V_{CC} are the highly promising candidate as catalysts for both OER and ORR, especially the non-noble metal catalyst Co-V_{CC} can be served as the efficient, stable and low-cost catalyst. Moreover, the catalyst is found to be electrically conductive. Our findings shed light on C₃N-based materials as efficient OER and ORR catalyst and offer a useful guide to select the active catalytic center of single-atom catalysts on 2D carbon nitride-based materials.

Conflicts of interest

There are no conflicts to declare.

Acknowledgements

This work was supported by the Assistant Secretary for Energy Efficiency and Renewal Energy of the U.S. Department of Energy under the Hydrogen Generation program. This theoretical work used the resources of the National Energy Research Scientific Computing Center (NERSC) that is supported by the Office of Science of the U. S. Department of Energy. We are

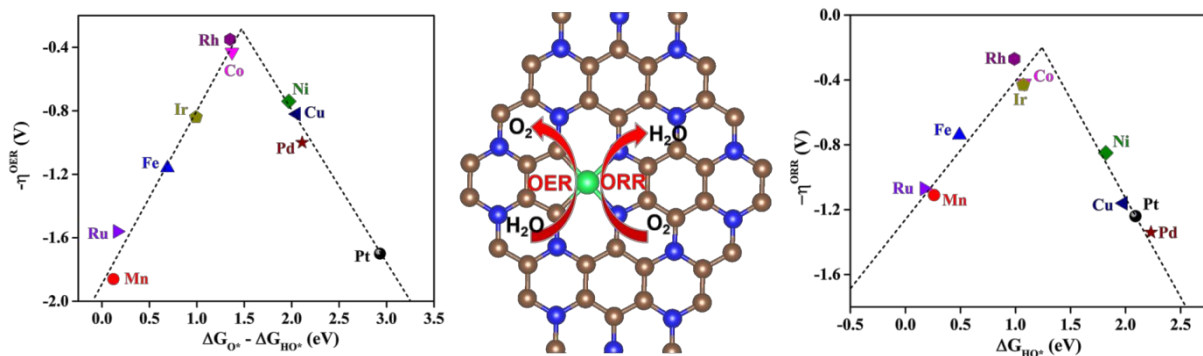
grateful to the Chinese Scholarship Council (CSC) for providing the Ph.D. scholarship and to Lawrence Berkeley National Laboratory (USA) for financial support.

Notes and references

1. M. S. Dresselhaus and I. L. Thomas, *Nat. Catal.*, 2001, **414**, 332–337.
2. N. L. Panwar, S. C. Kaushik and S. Kothari, *Renew. Sust. Energ. Rev.*, 2011, **15**, 1513–1524.
3. G. S. Liu, S. J. You, Y. Tan and N. Q. Ren, *Environ. Sci. Technol.*, 2017, **51**, 2339–2346.
4. A. B. Stambouli and E. Traversa, *Renew. Sust. Energ. Rev.*, 2002, **6**, 433–455.
5. G. P. Gao, Y. Jiao, F. X. Ma, Y. L. Jiao, E. Waclawik and A. J. Du, *J. Catal.*, 2015, **332**, 149–155.
6. Y. C. Lu, Z. C. Xu, H. A. Gasteiger, S. Chen, K. Hamad-Schifferli and Y. Shao-Horn, *J. Am. Chem. Soc.*, 2010, **132**, 12170.
7. Y. Jiao, Y. Zheng, M. Jaroniec and S. Z. Qiao, *Chem. Soc. Rev.*, 2015, **44**, 2060–2086.
8. E. A. Paoli, F. Masini, R. Frydendal, D. Deiana, C. Schlaup, M. Malizia, T. W. Hansen, S. Horch, I. E. L. Stephens and I. Chorkendorff, *Chem. Sci.*, 2015, **6**, 190–196.
9. J. Rossmeisl, Z. W. Qu, H. Zhu, G. J. Kroes and J. K. Nørskov, *J. Electroanal. Chem.*, 2007, **607**, 83–89.
10. N.M. Markovic, T. J. Schmidt, V. Stamenkovic', and P. N. Ross, *Fuel Cells*, 2001, **1**, 105–116.
11. X. Q. Huang, Z. P. Zhao, L. Cao, Y. Chen, E. B. Zhu, Z. Y. Lin, M. F. Li, A. M. Yan, A. Zettl, Y. M. Wang, X. F. Duan, T. Mueller and Y. Huang, *Science*, 2015, **348**, 1230–1234.
12. K. S. Novoselov, A. K. Geim, S. V. Morozov, D. Jiang, Y. Zhang, S. V. Dubonos, I. V. Grigorieva and A. A. Firsov, *Science*, 2004, **306**, 666–669.
13. X. P. Gao, Y. N. Zhou, Y. J. Tan, Z. W. Cheng, Q. I. Tang, J. P. Jia, and Z. M. Shen, *Energ. Fuel*, 2018, **32**, 5331–5337.
14. M. Shakourian-Fard, H. Heydari and G. Kamath, *Chemphyschem*, 2017, **18**, 2328–2335.
15. M. Naguib, V. N. Mochalin, M. W. Barsoum and Y. Gogotsi, *Adv. Mater.*, 2014, **26**, 992–1005.
16. B. Anasori, M. R. Lukatskaya and Y. Gogotsi, *Nat. Rev. Mater.*, 2017, **2**, 1–17.
17. J. C. Lei, X. Zhang and Z. Zhou, *Front. Phys.*, 2015, **10**, 107303.
18. H. O. Churchill and P. Jarillo-Herrero, *Nat Nanotechnol.*, 2014, **9**, 330–331.
19. Y. Li, F. Ma and L. W. Wang, *J. Mater. Chem. A.*, 2018, **6**, 7815–7826.
20. X. K. Kong, C. L. Chen and Q. W. Chen, *Chem. Soc. Rev.*, 2014, **43**, 2841–2857.
21. X. W. Wang, G. Z. Sun, P. Routh, D. H. Kim, W. Huang and P. Chen, *Chem. Soc. Rev.*, 2014, **43**, 7067–7098.
22. C. L. Tan, X. H. Cao, X. J. Wu, Q. Y. He, J. Yang, X. Zhang, J. Z. Chen, W. Zhao, S. K. Han, G. H. Nam, M. Sindoro and H. Zhang, *Chem. Rev.*, 2017, **117**, 6225–6331.
23. G. L. Chai, Z. F. Hou, D. J. Shu, T. Ikeda and K. Terakura, *J. Am. Chem. Soc.*, 2014, **136**, 13629–13640.
24. J. T. Zhang, Z. H. Zhao, Z. H. Xia and L. M. Dai, *Nat. Nanotechnol.*, 2015, **10**, 444–452.
25. W. Liang, J. X. Chen, Y. W. Liu and S. L. Chen, *ACS Catal.*, 2014, **4**, 4170–4177.
26. Y. N. Zhou, G. P. Gao, Y. Li, W. Chu and L. W. Wang, *Phys. Chem. Chem. Phys.*, 2019, **21**, 3024–3032.

27. S. C. Wang, Z. Y. Teng, C. Y. Wang and G. X. Wang, *ChemSusChem*, 2018, **11**, 2267-2295.
28. H. F. Wang, C. Teng and Q. Zhang, *Adv. Funct. Mater.*, 2018, **28**, 1803329-1803351.
29. P. Z. Chen, T. P. Zhou, L. L. Xing, K. Xu, Y. Tong, H. Xie, L. D. Zhang, W. S. Yan, W. S. Chu, C. Z. Wu and Y. Xie, *Angew. Chem. Int. Ed.*, 2017, **56**, 610-614.
30. X. F. YANG, A. Q. Wang, B. T. Qiao, J. Li, J. Y. Liu and T. Zhang, *Acc. Chem. Res.*, 2013, **46**, 1740-1748.
31. C. Z. Zhu, S. F. Fu, Q. R. Shi, D. Du and Y. H. Lin, *Angew. Chem. Int. Ed.*, 2017, **56**, 13944-13960.
32. J. Mahmood, E. K. Lee, M. Jung, D. B. Shin, H. J. Choi, J. M. Seo, S. M. Jung, D. Kim, F. Li, M. S. Lah, N. Park, H. J. Shin, J. H. Oh and J. B. Baek, *PNAS.*, 2016, **113**, 7414-7419.
33. X. D. Zhou, W. X. Feng, S. Guan, B. T. Fu, W. Y. Su and Y. G. Yao, *J. Mater. Res.*, 2017, **32**, 2993-3001.
34. Y. Hong, J. C. Zhang and X. C. Zeng, *Nanoscale.*, 2018, **10**, 4301-4310.
35. X. F. Li, L. Zhu, Q. Z. Xue, X. Chang, C. C. Ling and W. Xing, *ACS App. Mater. Interfaces.*, 2017, **9**, 31161-31169.
36. D. W. Ma, J. Zhang, X. X. Li, C. Z. He, Z. W. Lu, Z. S. Lu, Z. X. Yang and Y. X. Wang, *Sensor. Actuat. B-Chem.*, 2018, **266**, 664-673.
37. P. Bhauriyal, A. Mahata and B. Pathak, *J. Phys. Chem. C.*, 2018, **122**, 2481-2489.
38. J. T. Xu, J. Mahmood, Y. H. Dou, S. X. Dou, F. Li, L. M. Dai and J. B. Baek, *Adv. Mater.*, 2017, **29**, 1702007-1702015.
39. B. L. He, J. S. Shen, D. W. Ma, Z. S. Lu and Z. X. Yang, *J. Phys. Chem. C.*, 2018, **122**, 20312-20322.
40. M. Makaremi, B. Mortazavi and C. V. Singh, *J. Phys. Chem. C.*, 2017, **121**, 18575-18583.
41. H. I. Rasool, C. Ophus and A. Zettl, *Adv. Mater.*, 2015, **27**, 5771-5777.
42. F. Banhart, J. Kotakoski and A. V. Krasheninnikov, *ACS nano.*, 2011, **5**, 26-41.
43. Y. N. Tang, Z. X. Yang and X. Q. Dai, *J. Chem. Phys.*, 2011, **135**, 224704-224711.
44. X. F. Fan, W. T. Zheng and J. L. Kuo, *ACS App. Mater. Interfaces.*, 2012, **4**, 2432-2438.
45. G. P. Gao, E. R. Waclawik and A. J. Du, *J. Catal.*, 2017, **352**, 579-585.
46. T. W. He, S. K. Matta, G. Will and A. J. Du, *Small. Methods.*, 2019, 1800419.
47. X. Zhang, A. Chen, Z. H. Zhang, M. G. Jiao and Z. Zhou, *J. Mater. Chem. A.*, 2018, **6**, 11446-11452.
48. G. Kresse and J. Furthmuller, *Comput. Mater. Sci.*, 1996, **6**, 15-50.
49. G. Kresse and J. Furthmuller, *Phys. Rev. B: Condens. Matter Mater. Phys.*, 1996, **54**, 11169-11186.
50. P. E. Blöchl, *Phys. Rev. B: Condens. Matter Mater. Phys.*, 1994, **50**, 17953-17979.
51. J. P. Perdew, K. Burke and M. Ernzerhof, *Phys. Rev. Lett.*, 1996, **77**, 3865-3868.
52. J. P. Perdew, M. Ernzerhof and K. Burke, *J. Chem. Phys.*, 1996, **105**, 9982-9985.
53. S. Grimme, J. Antony, S. Ehrlich and H. Krieg, *J. Chem. Phys.*, 2010, **132**, 154104-154123.
54. H. J. Monkhorst and J. D. Pack, *Phys. Rev. B.*, 1976, **13**, 5188-5192.
55. G. Henkelman, B. P. Uberuaga and H. Jonsson, *J. Chem. Phys.*, 2000, **113**, 9901-9904.
56. G. Henkelman, A. Arnaldsson and H. Jonsson, *Comput. Mater. Sci.*, 2006, **36**, 354-360.
57. G. J. Martyna, M. L. Klein and M. Tuckerman, *J. Chem. Phys.*, 1992, **97**, 2635-2643.
58. K. Mathew, R. Sundararaman, K. Letchworth-Weaver, T. A. Arias and R. G. Hennig, *J. Chem. Phys.*, 2014, **140**, 084106-084114.
59. J. K. Nørskov, J. Rossmeisl, A. Logadottir and L. Lindqvist, *J. Phys. Chem. B.*, 2004, **108**, 17886-17892.
60. M. T. Li, L. P. Zhang, Q. Xu, J. B. Niu and Z. H. Xia, *J. Catal.*, 2014, **314**, 66-72.
61. P. Atkins and J. D. Paula, Oxford University Press, 2014.
62. H. D. Wang, H. Wu and J. L. Yang, *arXiv:1703.08754v1*, 2017.
63. Y. C. Ma, P. O. Lehtinen, A. S. Foster and R. M. Nieminen, *New. J. Phys.*, 2004, **6**, 68-83.
64. A. A. El-Barbary, R. H. Telling, C. P. Ewels, M. I. Heggie and P. R. Briddon, *Phys. Rev. B.*, 2003, **68**, 144107-144114.
65. D. W. Ma, J. Zhang, Y. N. Tang, Z. M. Fu, Z. X. Yang and Z. S. Lu, *Phys. Chem. Chem. Phys.*, 2018, **20**, 13517-13527.
66. Y. N. Zhou, W. Chu, F. L. Jing, J. Zheng, W. J. Sun and Y. Xue, *Appl. Surf. Sci.*, 2017, **410**, 166-176.
67. H. Tang and S. Ismail-Beigi, *Phys. Rev. Lett.*, 2007, **99**, 115501-115505.
68. H. X. Xu, D. J. Cheng, D. P. Cao and X. C. Zeng, *Nat. Catal.*, 2018, **1**, 339-348.
69. M. Mavrikakis, B. Hammer and J. K. Nørskov, *Phys. Rev. Lett.*, 1998, **81**, 2819-2822.
70. B. Hammer, J. K. Nørskov, *Adv. Catal.*, 2000, **45**, 71-129.
71. J. R. Kitchin, J. K. Nørskov, M. A. Barteau and J. G. Chen, *Phys. Rev. Lett.*, 2004, **93**, 156801-156805.
72. V. Stamenkovic, B. S. Mun, K. J. J. Mayrhofer, P. N. Ross, N. M. Markovic, J. Rossmeisl, J. Greeley and J. K. Nørskov, *Angew. Chem. Int. Ed.*, 2006, **118**, 2963-2967.
73. Y. Y. Liu, Y. M. Wang, B. I. Yakobson and B. C. Wood, *Phys. Rev. Lett.*, 2014, **113**, 028304-028309.
74. F. Calle-Vallejo, A. Krabbe and J. M. Garcia-Lastra, *Chem. Sci.*, 2017, **8**, 124-130.
75. M. T. de Groot and M. T. Koper, *Phys. Chem. Chem. Phys.*, 2008, **10**, 1023-1031.
76. C. Y. Ling, L. Shi, Y. X. Ouyang, X. C. Zeng and J. L. Wang, *Nano. Lett.*, 2017, **17**, 5133-5139.
77. J. K. Nørskov, T. Bligaard, A. Logadottir, J. R. Kitchin, J. G. Chen, S. Pandalov and U. Stimming, *J. Electrochem. Soc.*, 2005, **152**, J23-J26.
78. I. C. Man, H. Y. Su, F. Calle-Vallejo, H. A. Hansen, J. I. Martínez, N. G. Inoglu, J. Kitchin, T. F. Jaramillo, J. K. Nørskov and J. Rossmeisl, *ChemCatChem.*, 2011, **3**, 1159-1165.
79. J. Rossmeisl, A. Logadottir and J. K. Nørskov, *Chem. Phys.*, 2005, **319**, 178-184.

Graphical Abstract



The best TM atom for OER is Rh- V_{CC} with η^{OER} of 0.35 V, followed by Co- V_{CC} (0.43 V), and for ORR, Rh- V_{CC} exhibits the lowest η^{ORR} of 0.27 V, followed by Co- V_{CC} (0.42 V).

Graphical abstract

Transition metal embedded two-dimensional C_3N as highly active electrocatalysts for oxygen evolution and reduction reactions

Yanan Zhou,^{ab} Guoping Gao,^b Jun Kang,^c Wei Chu,^{*a} and Lin-Wang Wang^{*b}

^a School of Chemical Engineering, Sichuan University, Chengdu, 610065, Sichuan, China

^b Materials Science Division, Lawrence Berkeley National Laboratory, Berkeley, 94720, California, United States

The best TM atom for OER is Rh- V_{CC} with η^{OER} of 0.35 V, followed by Co- V_{CC} (0.43 V), and for ORR, Rh- V_{CC} exhibits the lowest η^{ORR} of 0.27 V, followed by Co- V_{CC} (0.42 V).

